

Multi-task Geometric Estimation of Depth and Surface Normal from Monocular 360° Images

Kun Huang¹, Fang-Lue Zhang¹(✉), Fangfang Zhang¹, Yu-Kun Lai², Paul Rosin², and Neil A. Dodgson¹

© The Author(s)

Abstract Geometric estimation is required for scene understanding and analysis of panoramic 360° images. Current methods usually predict a single feature, such as depth or surface normal. These methods can lack robustness, especially when dealing with intricate textures or complex object surfaces. We introduce a novel multi-task learning (MTL) network that simultaneously estimates depth and surface normals from 360° images. Our first innovation is our MTL architecture, which enhances predictions for both tasks by integrating geometric information from depth and surface normal estimation, enabling a deeper understanding of 3D scene structure. Another innovation is our fusion module, which bridges the two tasks, allowing the network to learn shared representations that improve accuracy and robustness. Experimental results demonstrate that our MTL architecture significantly outperforms state-of-the-art methods in both depth and surface normal estimation, showing superior performance for complex and diverse scenes. Our model's effectiveness and generalizability, particularly in handling intricate surface textures, establish it as a new benchmark for 360° image geometric estimation. The code and model are available at <https://github.com/huangkun101230/360MTLGeometricEstimation>.

Keywords 360° images, depth estimation, surface normal estimation, multi-task learning

1 Introduction

Multi-task learning (MTL) has emerged as a powerful approach to computer vision. By simultaneously tackling inherently related tasks, MTL leverages shared representations to enhance overall performance, robustness, and generalization across all tasks [1, 2]. We apply MTL to monocular 360° images, simultaneously predicting depth and surface normals. The 360° depth estimation provides holistic scene information that covers the 360° × 180° field of view (FoV), while 360°

surface normal estimation gives insights into the orientation of surfaces within the scene [3]. When these tasks are learned together, the model can develop a fuller understanding of the scene's 3D structure, as each task reinforces the other. For instance, accurate depth estimation can inform surface normal prediction by providing context about the relative positioning of objects, while precise surface normal estimation can refine depth predictions by offering additional geometric cues. This synergy between tasks not only enhances the overall accuracy of the model but also improves its ability to generalize to new environments, making MTL for depth and surface normal estimation an important strategy in advancing state-of-the-art computer vision systems, such as those used in indoor navigation for cleaning robots. By jointly estimating depth and surface normals, such robots can more effectively understand object distances and surface orientations, enabling them to navigate complex environments efficiently and safely.

Conventional depth estimation methods that rely on perspective images struggle with geometric distortions introduced by mapping the entire scene onto equirectangular projection (ERP) images, which is the most commonly used format for storing and displaying 360° imagery. These distortions, most severe along the vertical axis and intensifying towards the poles, make it challenging for traditional perspective methods to effectively extract features directly from the ERP domain. Previous methods [4, 5] address this problem by extracting reliable features with distortion-aware convolu-

1 School of Engineering and Computer Science, Victoria University of Wellington, Wellington, New Zealand. E-mail: Kun Huang, kun.huang@vuw.ac.nz; Fanglue Zhang, fanglue.zhang@vuw.ac.nz; Fangfang Zhang, fangfang.zhang@vuw.ac.nz; Neil Dodgson, neil.dodgson@vuw.ac.nz. Fang-Lue Zhang is the corresponding author.

2 School of Computer Science and Informatics, Cardiff University, Cardiff, UK. Email: Rosin, RosinPL@cardiff.ac.uk; Y.-K. Lai, Yukun.Lai@cs.cardiff.ac.uk.

Manuscript received: 2022-01-01; accepted: 2022-01-01

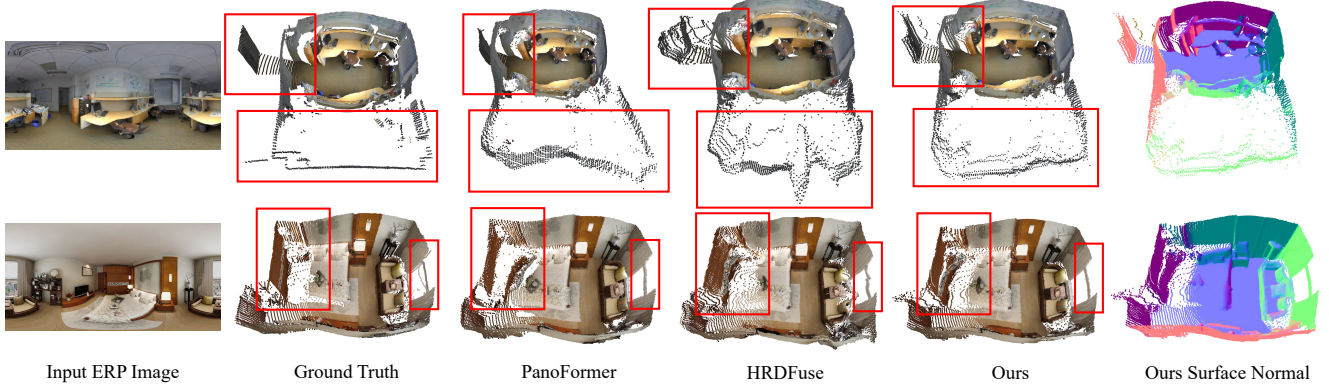


Fig. 1 Our MTL model provides more accurate geometric estimates for 360° images than other methods, particularly in the regions highlighted by red rectangles. The results are visualized as 3D point clouds, with both RGB data and color-coded surface normal maps.

tions and spherical kernels but add computational complexity and often miss global spatial relationships due to the local nature of convolutional kernels. Alternative approaches [6–8] mitigate distortion through different projections, while other models [9–11] rely on Vision Transformers (ViTs) to address projection discrepancies and interpret scenes using patch-wise information. However, these methods often struggle to accurately discern coherent surface regions, particularly in areas that are severely distorted by the spherical projection near the poles of the ERP image. This difficulty is exacerbated by subtle texture variations or repeated patterns, which existing depth estimation techniques struggle to capture accurately. Consequently, depth maps often smooth over these variations, leading to a loss of critical geometric details. While surface normal maps can offer supplementary information to help with these challenges, the integration of depth and surface normal estimation tasks has been under-explored in the 360° domain. A multi-task learning approach, in which depth and surface normal predictions support and refine each other, can improve results for both tasks. This approach allows for more accurate depth maps that retain essential geometric details and surface normal maps that are more precise, ultimately enhancing the model’s overall geometric understanding of the 3D scene.

This paper introduces a novel end-to-end deep architecture that uses a multi-task learning strategy for monocular 360° depth estimation by simultaneously learning surface normals. Inspired by the findings of Standley et al. [2], which demonstrate that surface normal estimation enhances other tasks in multi-task learning, our approach integrates depth and surface normal predictions to improve overall accuracy.

The proposed network comprises three key components to address distortion issues and enhance depth and surface normal predictions through task knowledge transfer. First,

a shared feature extractor generates features for both depth and surface normal branches, which are processed by two separate spherical distortion-aware ViT networks to address the spherical distortion challenges inherent in 360° imagery. Second, we introduce a novel fusion mechanism that enables knowledge transfer between the spherical ViTs by integrating feature maps from each task. This fusion enhances scene geometry comprehension and improves depth map predictions. Third, task-specific multi-scale transformer decoders are used to handle long-range dependencies, significantly boosting prediction accuracy across various scales.

By simultaneously learning depth and surface normals, our model achieves a more comprehensive understanding of scene structure and geometry, resulting in improved recognition and interpretation of object shapes and spatial relationships, as shown in Fig. 1. For instance, our model consistently provides clearer segmentation and more accurate geometric details, even in complex regions. The model excels at capturing fine-grained scene structures, which are essential for accurately interpreting depth and surface normals in challenging environments. The insights provided by surface normals enhance the spatial continuity and geometric details of depth estimation, particularly in the areas highlighted by the red rectangles. Additionally, our spherical ViT networks enrich scene comprehension by offering a detailed view of the 3D structure and object layout in panoramic scenes. Extensive experiments demonstrate that our model significantly outperforms state-of-the-art algorithms in both 360° depth and surface normal estimation, with strong generalization in real-world test cases. The contributions of this paper are as follows:

- a novel monocular 360° MTL architecture for estimating both depth and surface normals which outperforms state-of-the-art algorithms for both tasks,

- a fusion module designed to efficiently merge 360° features in the context of depth and surface normal learning, with sharing between tasks, leading to enhanced scene structure understanding and improved model generalizability, and
- comprehensive experimental evaluation of the generalization capability and robustness of our method in depth and surface normal estimation, with comparisons to state-of-the-art approaches across diverse scenes and datasets. The results reveal that our method consistently outperforms existing approaches on widely recognized benchmarks while maintaining a similar computation time to single-task methods.

2 Related Work

2.1 Monocular 360° Depth Estimation

Various approaches have been taken to tackle the spherical distortion present in ERP imagery for 360° depth estimation. Some methods [12–14] directly take the ERP image as input, employing conventional convolutional filters to perceive the spherical distortion field and use other intrinsic information of the scene, such as the indoor layout structure, to model the final depth map. In contrast, Liao et al. [4] and Coors et al. [5] used distortion-adapted kernels to enable formal convolution operations on ERP images. However, such methods often demand significant computational effort, and their effectiveness remains less explored. More recently, bi-projection has emerged as an increasingly popular approach to addressing distortion challenges. This technique involves projecting the distorted image onto a suitable intermediate representation and then reprojecting it back to the original domain. Approaches such as GLPanoDepth [15], BiFuse [6], BiFuse++ [7], and UniFuse [8] incorporate both ERP and CP during neural network training. Specifically, BiFuse uses fusion in both the encoder and decoder stages, while others share the fused features only at the encoder stage. Recently, tangent projection (TP) has shown potential to address distortion challenges. This is because the transformed patches under TP have smaller FoVs and less distortion compared to the cube faces. For example, 360MonoDepth [16] directly applies a pre-trained perspective depth estimator to project tangent patches and fuses them back into the ERP image to obtain the final depth map. OmniFusion [9], PanoFormer [10] and HRDFuse [11] apply transformer-based architectures to embed geometric information from tangent patches for depth estimation. Recently, Elite360D [17] introduced the use of icosahedron projection to enhance geometric information, while Liu et al. [18] employed a teacher-student architec-

ture to generate comprehensive features for depth estimation. However, approaches that focus solely on depth estimation can result in models that are less robust and have a limited understanding of scene structure. Single-task learning risks overfitting to specific details and missing crucial information about surface orientation and spatial relationships.

2.2 Monocular 360° Surface Normal Estimation

While surface normal estimation has been extensively studied for perspective images, directly applying these methods [3, 19–22] to the 360° domain often yields unsatisfactory results due to spherical distortion. Although 360° surface normal estimation can provide comprehensive information to enhance geometric awareness, it has been less explored than 360° depth estimation. Karakottas et al. [23] introduced HyperSphere, a state-of-the-art method for estimating surface normals in the 360° domain. This approach uses a quaternion loss for supervising surface normal predictions within a CNN architecture. However, their experiments did not cover widely used datasets in the 360° domain, limiting applicability and preventing it from establishing a standard similar to that for 360° depth estimation. Additionally, the CNN model struggles to efficiently extract features from ERP imagery; relying solely on surface normal supervision can make predictions sensitive to subtle texture or color changes, obstacles that can be mitigated by incorporating depth information.

2.3 Multi-task Learning for Image Regression

Multi-task learning is a form of transfer learning, that addresses multiple tasks simultaneously by leveraging shared domain knowledge across complementary tasks [2, 24]. For image regression tasks in computer vision, numerous methods [25–28] adopt a multi-task strategy to concurrently predict various related outputs, including depth [29], optical flow [30], scene flow [31], semantic segmentation [32], and other data [33, 34], yielding promising results. Recent works have explored different sharing methods for effective knowledge transfer within neural networks, either by manipulating hidden layers or dynamically balancing losses during back-propagation. Approaches such as hard parameter-sharing [28, 32, 35] involve a pipeline with a single encoder and multiple decoders for each task. In contrast, soft parameter-sharing [26, 36] uses multiple network columns for each task, defining a strategy to share features between columns. Sun et al. [37] introduce an adaptive method for learning the sharing pattern in multi-task networks, employing a task-specific policy for separate execution paths within a single neural network while still using standard

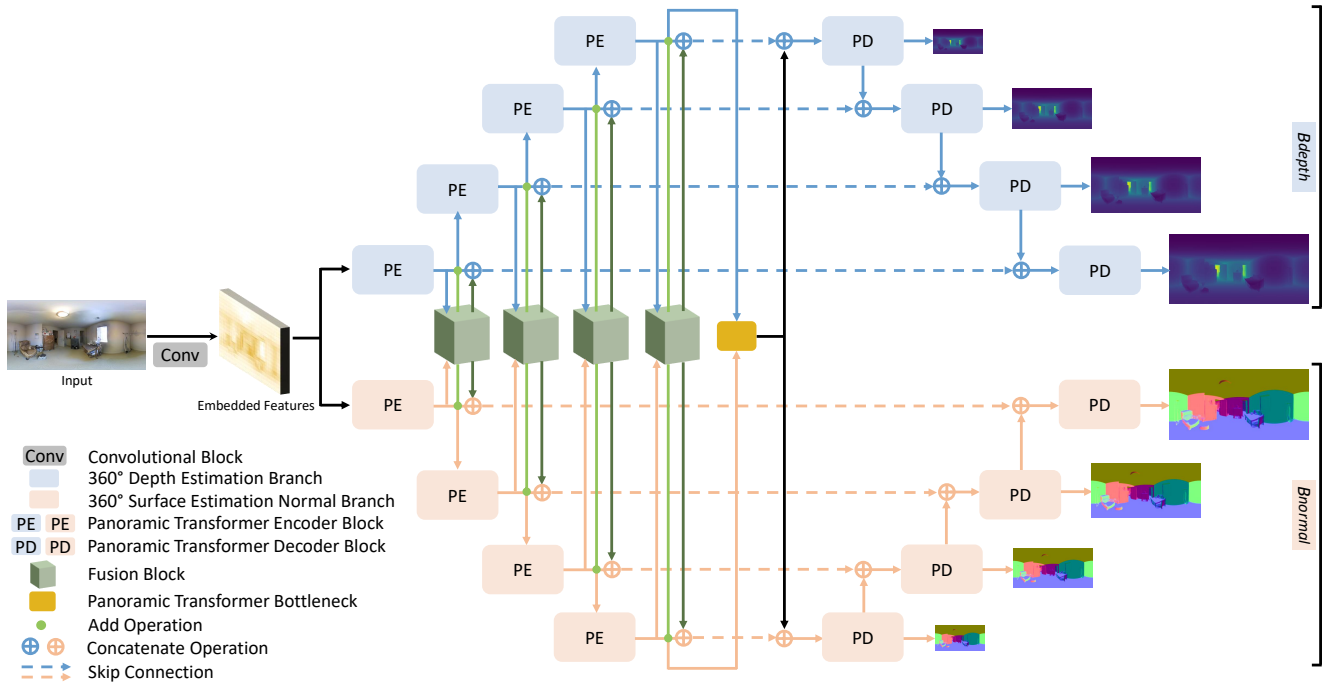


Fig. 2 Our network architecture has two branches: B_{depth} (blue) and B_{normal} (red), dedicated to depth and surface normal estimation, respectively. A fusion module (green) is employed to fuse the feature maps between each encoder level of B_{depth} and B_{normal} and feed the fused features into the next encoder level. The fused features are also concatenated with the original depth or normal features and fed to the corresponding decoder blocks. The final depth and normal maps are predicted in a multi-scale manner.

back-propagation. Conversely, others [28, 38] have explored an adaptive approach to guide the weights of the losses during back-propagation in MTL. The established potential and effectiveness of ViT for 360° vision tasks, and the promise of MTL to improve performance through shared representations, motivated us to explore a multi-task ViT architecture specifically for ERP imagery. By concurrently estimating depth and surface normals, this architecture employs a soft parameter-sharing strategy, which improves robustness and adaptability in diverse scenarios, leading to more accurate 360° depth and surface normal estimation.

3 Methodology

3.1 Architecture

Our MTL architecture leverages the learned representations from both depth and surface normal estimation; this enhances overall scene understanding and improves the accuracy of both tasks. Depth estimates provide crucial spatial information, while surface normals contribute detailed insights into object perception and surface orientations within a scene. The interaction between these complementary tasks is facilitated by a specially designed fusion block, which promotes seamless integration of information from both tasks. This bidirectional enhancement allows the model to achieve superior performance in both depth and surface normal estimation,

leading to a more comprehensive and accurate understanding of the scene. To address the challenges posed by spherical distortion in 360° images, we developed a U-shaped MTL architecture that incorporates distortion-aware ViT blocks, built on the foundation of PanoFormer [10]: the panoramic transformer encoder and decoder blocks (PE and PD) in Fig. 2. Our transformer decoder incorporates a multi-level structure, focusing on spatial interconnections, handling intricate regional details, and fusing contextual information at varying scales. This hierarchical transformer architecture is applied to both depth and surface normal tasks, resulting in two distinct ViT networks. These networks exchange knowledge by soft-parameter sharing [39] between their encoders through the fusion block at corresponding scales at each level.

An overview of our proposed network is shown in Fig. 2. It simultaneously learns to predict depths and surface normals using a hierarchical structure, comprising a shared convolutional feature embedding block, fusion blocks, bottleneck, and multi-scale spherical encoders and decoders with spherical distortion awareness. The shared convolutional feature embedding block includes 3×3 convolutional layers and a 2×2 max pooling layer. It aims to extract contextual and salient features from input images for both tasks. Furthermore, employing such a down-sampling layer is crucial to improving computational efficiency and reducing the number

of parameters in our multi-task model. The down-sampled features are directed into two branches (B_{depth} and B_{normal}) concurrently. Each branch comprises encoders and decoders and is organized into four hierarchical stages that either halve or double the dimensions and resolution of features. The feature maps of B_{depth} and B_{normal} are fused through our proposed fusion module at each encoding stage. Finally, the decoder leverages concatenated features from corresponding encoders, fusion modules and decoded feature maps to extract multi-scale depth or surface normal features, followed by an up-sampling step to reconstruct the depth and normal maps at full resolution.

3.2 Panoramic Transformer Block

The primary issue in processing panoramic images is the distortion introduced by ERP projection, which differs significantly from the distortion found in perspective images due to the non-uniform spatial warping of features. While our focus is on developing an effective MTL architecture, we adopt the PanoFormer block proposed by Shen et al. [10] to specifically address this distortion issue. Unlike conventional transformer-based methods that sample features linearly from the input, PanoFormer leverages tangent projection to convert ERP images into a set of tangent patches, each centered on a specific point in the image. By focusing on the pixels surrounding each tangent plane's center, this method captures spherical geometric information more effectively, as the tangent patches avoid the distortions typically present in ERP images, allowing for more accurate feature extraction from 360° imagery. Additionally, this encoder block is enhanced by a locally-optimized feed-forward network [40], which strengthens local feature interactions within each patch, ensuring that fine-grained details are preserved. The encoder also models token flow relationships between the centers of the tangent patches, enabling the network to understand and capture global dependencies across the entire image. This combination of local refinement and global awareness allows the spherical encoder to better handle the complexities of spherical geometry in 360° images. The representation of the self-attention mechanism is:

$$P(f, \hat{s}) = \sum_m W_m \left[\sum_{(q,k)} A_{mqk} W'_m f(\hat{s}_{mqk} + \Delta s_{mqk}) \right] \quad (1)$$

where the feature representations f undergo spherical sampling (denoted \hat{s}), involving self-attention heads (m), individual tokens (q), and their neighboring tokens within a tangent patch (k). Learnable weights for each head are denoted by

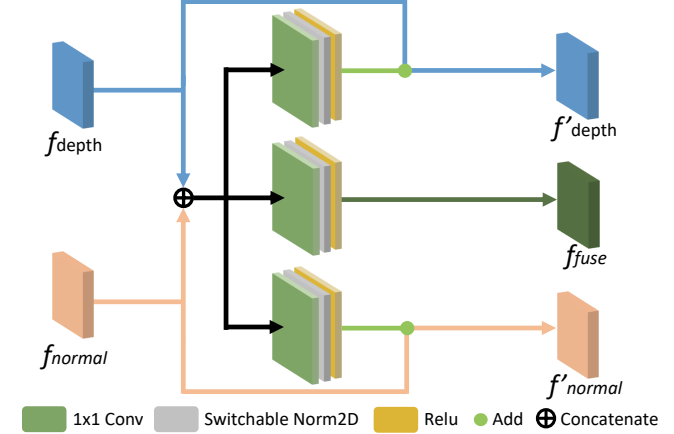


Fig. 3 Our proposed fusion module for fusing 360° depth and surface normal features.

W_m and W'_m , while A_{mqk} indicates the attention weights assigned to each token, and Δs_{mqk} represents the learned flow for individual tokens.

3.3 Fusing Depth and Surface Normal Features

Our fusion module is designed to efficiently extract representations for the two complementary tasks, seamlessly integrated with ViT networks, as depicted in Fig. 3. Our fusion module draws inspiration from BiFuse++ [7]. It comprises three blocks, each with an identical structure. Within each block, we employ three convolutional layers: a 1×1 convolutional layer, a switchable normalization layer (SwitchableNorm), and a ReLU activation function. Conventional convolutional blocks typically use batch normalization [41] to mitigate internal covariate shifts. However, since our network contains both convolutional layers (in fusion blocks) and panoramic ViTs (in main branches), uniformly applying batch normalization and layer normalization is sub-optimal for our learning task. Therefore, we adopt switchable normalization [42] that learns weights for channel-wise, layer-wise, and batch-wise normalization to adaptively control the behaviour of the normalization layer. By flexible selection of the most effective normalization strategy for different components and the information learned from different tasks, employing switchable normalization improves the generalization capability and performance of our deep model relative to using a fixed normalization method.

Our fusion module takes the concatenation of depth features (f_{depth}) and surface normal features (f_{normal}) as input from their respective task branches. This concatenated feature is processed through three individual blocks, each dedicated to learning distinct representations. For the depth block (blue in Fig. 3) and the surface normal block (red in Fig. 3), each

of the two branches predicts a residual map that incorporates additional information from the other task to refine its feature maps. The resulting feature maps (f'_{depth} and f'_{normal}) are then propagated to the next encoder level and simultaneously linked to the corresponding decoder block, where they are concatenated with the fused feature map (f_{fuse}) from the fusion block. Our fusion module offers several advantages: it facilitates mutual information sharing, allowing each task to benefit from insights gained by the other; it enables the model to adapt to task-specific challenges, focusing on regions where one task provides more reliable information; and it enhances robustness and generalization ability by reducing sensitivity to noise or inaccuracies in a single task, leading to improved performance across diverse scenes.

3.4 Multi-scale Spherical Encoding and Decoding

The proposed ViT decoder (\hat{P}) addresses spherical distortion, comprising the same number of blocks as the encoder for each task. It predicts the depth (\hat{D}_i) or surface normal map (\hat{N}_i) at various scales (denoted i). Each block takes as input the concatenation of the upsampled encoded representations, \hat{f}_i , which has half the number of channels and double the spatial resolution of the previous block. This input is further combined with the task-specific feature and the fused feature through skip-links. After each block, the predictions are produced at various scales using a 3×3 convolution operation followed by bilinear interpolation to double the output size. Each task-specific prediction is then passed through a corresponding activation function to constrain the output to lie within its valid range. For instance, sigmoid activation (σ) is applied to the depth map to limit values between 0 and 1, while tanh activation (tanh) is used for the surface normal map to constrain values within the range $[-1, 1]$. In our experiments, the model failed to converge during training without use of these two activation functions. The process is:

$$\hat{D}_i = \sigma \left(\hat{P}_{\text{depth}}(\hat{f}_{\text{depth},i} \oplus f'_{\text{depth},i} \oplus f_{\text{fuse},i}) \right) \quad (2)$$

$$\hat{N}_i = \tanh \left(\hat{P}_{\text{normal}}(\hat{f}_{\text{normal},i} \oplus f'_{\text{normal},i} \oplus f_{\text{fuse},i}) \right) \quad (3)$$

Our multi-scale decoder offers a range of advantages. Processing information at various spatial levels of the panoramic scene enables the network to capture both fine details and global context for depth estimation. This adaptability to different object sizes ensures that the network can effectively represent structures at varying scales, promoting robustness to diverse objects. By interpreting the fused feature in a multi-scale manner, a richer representation of the inherent geometric information can be learned, which is valuable for the task of

depth estimation. Moreover, the model's generalizability to different panoramic scene layouts is enhanced, reducing the risk of over-fitting common scene structures present in the training data.

The effectiveness of these introduced components is confirmed through our ablation study (see Sec. 4.7).

3.5 Loss Function

Our proposed MTL network simultaneously predicts depth and surface normal maps across S scales (S is set to 4 in our experiments), aiming to capture a comprehensive and holistic representation of the scene geometry. During training, we focus on measuring the loss only for valid pixels; the number of such pixels is denoted M . The formulated loss functions are as follows.

3.5.1 MSE Loss

$\mathcal{L}_{\text{Dmse}}$ and $\mathcal{L}_{\text{Nmse}}$ represent the mean squared error of the estimated map for the two tasks, and are defined as:

$$\begin{aligned} \mathcal{L}_{\text{Dmse}} &= \sum_{j=1}^M \|\Delta_D\|_2 \\ \mathcal{L}_{\text{Nmse}} &= \sum_{i=1}^S \sum_{j=1}^M \|\Delta_N\|_2 \end{aligned} \quad (4)$$

where $\Delta_D = \hat{D}_j - D_j$, \hat{D}_j represents the predicted depth, and D_j is the ground truth map at the finest scale for the current valid pixel j . $\Delta_N = \arccos(\hat{N}_{ij} \cdot N_{ij})$ denotes angular difference.

3.5.2 Quaternion Loss

$\mathcal{L}_{\text{quat}}$ [23] measures the angular difference between predicted and ground truth normal maps on per-pixel basis:

$$\mathcal{L}_{\text{quat}} = \sum_{i=1}^S \sum_{j=1}^M \arctan \left(\frac{\|\hat{N}_{ij} \times N_{ij}\|}{\hat{N}_{ij} \cdot N_{ij}} \right) \quad (5)$$

3.5.3 Perceptual Loss

$\mathcal{L}_{\text{Dperc}}$ and $\mathcal{L}_{\text{Nperc}}$ are applied at the finest scale to improve the generation of intricate details in both depth and surface normal predictions:

$$\begin{aligned} \mathcal{L}_{\text{Dperc}} &= \sum_{j=1}^M l_{\text{feat}}^{\phi,k}(\hat{D}_j, D_j) \\ \mathcal{L}_{\text{Nperc}} &= \sum_{j=1}^M l_{\text{feat}}^{\phi,k}(\hat{N}_j, N_j) \end{aligned} \quad (6)$$

$$l_{\text{feat}}^{\phi,k}(\text{pred}, \text{gt}) = \frac{1}{C_k M} \|\phi_k(\text{pred}_j) - \phi_k(\text{gt}_j)\|_2^2 \quad (7)$$

where C denotes the feature's dimensionality, ϕ represents the pre-trained VGG16 network [43], and k is the k -th layer within the network ϕ .

3.5.4 Gradient Loss

Gradient loss is formulated as:

$$\mathcal{L}_{\text{grad}} = \sum_{s=1}^S \frac{1}{M} \sum_{i=1}^M \left(\left| \nabla D_s^i - \nabla \hat{D}_s^i \right| \right) \quad (8)$$

where ∇ represents the sum of the mean absolute differences between the gradients of the predicted depth map and the ground truth maps, computed using Sobel kernel convolutions.

3.5.5 Overall Loss

The overall loss $\mathcal{L}_{\text{total}}$ function of our network is defined as:

$$\begin{aligned} \mathcal{L}_{\text{total}} = & \lambda_{\text{Dmse}} \mathcal{L}_{\text{Dmse}} + \lambda_{\text{grad}} \mathcal{L}_{\text{grad}} + \\ & \lambda_{\text{Dperc}} \mathcal{L}_{\text{Dperc}} + \lambda_{\text{Nmse}} \mathcal{L}_{\text{Nmse}} + \\ & \lambda_{\text{quat}} \mathcal{L}_{\text{quat}} + \lambda_{\text{Nperc}} \mathcal{L}_{\text{Nperc}} \end{aligned} \quad (9)$$

We assign weights to the depth terms as follows: $\lambda_{\text{Dmse}} = 2.0$, $\lambda_{\text{grad}} = 1.0$, and $\lambda_{\text{Dperc}} = 0.05$. For surface normal terms, we set $\lambda_{\text{Nmse}} = 1.0$, $\lambda_{\text{quat}} = 10.0$, and $\lambda_{\text{Nperc}} = 0.05$. Through our experiments, we noted that employing this specific combination of investigated loss functions and corresponding weights consistently led to superior outcomes when compared to alternative combinations. This observation carries significant importance in the context of MTL, as an imbalanced adjustment of loss weights or the use of inappropriate loss functions may result in one task dominating another. Moreover, such misalignments can even lead to the failure of the model to converge, underscoring the critical role of carefully selecting and weighting loss functions for successful multi-task training.

4 Experiments and Results

4.1 Methodology

We have validated our method on five widely recognized panoramic benchmark datasets: 3D60 [14], Structured3D [44], Stanford2D3D [45], Matterport3D [46], and SunCG [47]. Both quantitative and qualitative evaluations were conducted for depth and surface normal estimation tasks, comparing our approach to state-of-the-art methods in both the 360° and perspective domains. Given the limited previous work on MTL models in the 360° domain, our comparisons primarily consider existing single-task learning methods. For 360° depth estimation, we compare our model to GLPanoDepth [15], PanoFormer [10], HRDFuse [11], and UniFuse [8]. For 360° surface normal estimation, we compare to the current state-of-the-art, HyperSphere [23], and adapt the prediction layers of UniFuse, PanoFormer, and OmniFusion [9] to enable surface normal estimation, allowing for a direct comparison of network architectures. There are no prior MTL models designed for 360° imagery; therefore,

to provide a comparison against an existing MTL model, we retrained the recently-published perspective-based MTL method ASNGeo [3] using 360° data for both tasks. We have also conducted an ablation study to assess the key components of our approach, focusing on the depth estimation task, and we have further evaluated the speed of our method.

4.2 Evaluation Metrics

We assessed the performance of depth estimation using four standard error metrics: mean absolute error (MAE), absolute relative error (ARE), root mean square error (RMSE), and logarithmic root mean square error (RMSElog). Additionally, we used three accuracy metrics to evaluate the percentage of pixels where the ratio (δ_D) of the difference between the predicted depth map and the ground truth is less than 1.25¹, 1.25², and 1.25³. For surface normal estimation, we used three standard error metrics: mean error, median error, and mean square error (MSE), along with five accuracy metrics that measure the percentage of pixels where the angular difference (δ_N) between the predicted normals and the ground truth is less than 5°, 7.5°, 11.25°, 22.5°, and 30°. To ensure fair comparisons, we applied consistent experimental settings to all methods.

4.3 Datasets

—The following datasets were used for evaluation.

4.3.1 3D60 Dataset

3D60 is a panoramic dataset encompassing RGB, depth, and surface normal data at resolutions of 256 × 512, captured for diverse scenes. It is based on two real-world indoor scanning setups, Stanford2D3D and Matterport3D, and a synthetic dataset from SunCG, introducing an inherent distribution gap for improved model generalizability. We followed the data split in HyperSphere, as recommended in the authors' introduction. It is important to note that Matterport3D lacks ground truth for surface normals, and Stanford2D3D's surface normal maps lack consistently aligned vector directions across their data. Additionally, 3D60 faces limitations in rendering imagery that could impact the depth estimation task. As a result, our evaluations focused on specific subsets within the 3D60 dataset.

4.3.2 Structured3D Dataset

Structured3D constitutes an extensive synthetic dataset, comprising 21,835 panoramic data instances at a resolution of 512 × 1024 for 3500 scenes. The dataset includes RGB images illuminated with cold, normal, and warm lighting, along with various annotations, such as depth, surface normal, and

Table 1 360° depth estimate results on five benchmarks. We compare our method to state-of-the-art approaches, highlighting improvements over existing best results for each error and accuracy metric as ‘Ours-Improved by’.

* Indicates evaluation performed using the corresponding partitions of the 3D60 dataset.

Dataset	Method	Error metric ↓				Accuracy metric ↑		
		MAE	ARE	RMSE	RMSElog	δ_{D1}	δ_{D2}	δ_{D3}
3D60	UniFuse	0.1611	0.0720	0.3012	0.0464	94.51	98.87	99.64
	PanoFormer	0.1244	0.0617	0.2234	0.0386	96.65	99.41	99.80
	HRDFuse	0.1611	0.0729	0.2911	0.0460	94.72	98.92	99.62
	GLPanoDepth	0.1426	0.0673	0.2535	0.0420	96.00	99.30	99.79
	ASNGeo	0.1782	0.0837	0.3305	0.0525	93.24	98.68	99.59
	Ours	0.0962	0.0465	0.2050	0.0325	97.66	99.50	99.83
	Ours-Improved by	22.67%	24.64%	8.24%	15.80%	1.01	0.09	0.03
Stanford2D3D*	UniFuse	0.1539	0.0683	0.2884	0.0462	95.08	99.07	99.72
	PanoFormer	0.1099	0.0537	0.2043	0.0363	97.29	99.61	99.89
	HRDFuse	0.1396	0.0614	0.2606	0.0412	96.39	99.41	99.81
	GLPanoDepth	0.1530	0.0716	0.2599	0.0442	95.89	99.45	99.85
	ASNGeo	0.1627	0.0790	0.3051	0.0515	93.51	99.01	99.71
	Ours	0.0873	0.0418	0.1928	0.0315	98.02	99.67	99.88
	Ours-Improved by	20.56%	22.16%	5.63%	13.22%	0.73	0.06	-0.01
Matterport3D*	UniFuse	0.1759	0.0772	0.3190	0.0483	94.22	98.96	99.70
	PanoFormer	0.1348	0.0657	0.2360	0.0399	96.78	99.50	99.88
	HRDFuse	0.1719	0.0764	0.3022	0.0469	94.93	99.16	99.75
	GLPanoDepth	0.1515	0.0709	0.2627	0.0430	96.12	99.38	99.83
	ASNGeo	0.1866	0.0869	0.3406	0.0536	93.32	98.71	99.63
	Ours	0.1035	0.0486	0.2141	0.0331	97.74	99.59	99.87
	Ours-Improved by	23.22%	26.03%	9.28%	17.04%	0.96	0.09	-0.01
SunCG*	UniFuse	0.1071	0.0540	0.2401	0.0392	95.19	98.32	99.30
	PanoFormer	0.0969	0.0534	0.1890	0.0354	94.87	98.83	99.51
	HRDFuse	0.1366	0.0690	0.2744	0.0465	92.15	97.42	98.89
	GLPanoDepth	0.0957	0.0486	0.2094	0.0361	95.60	98.82	99.54
	ASNGeo	0.1588	0.0752	0.3132	0.0489	92.63	98.22	99.31
	Ours	0.0718	0.0405	0.1756	0.0303	97.14	99.04	99.60
	Ours-Improved by	24.97%	16.67%	7.09%	14.41%	1.54	0.21	0.06
Structured3D	UniFuse	0.2581	0.2149	0.4133	0.1142	75.25	91.09	95.61
	PanoFormer	0.3097	0.2697	0.4804	0.1283	71.84	88.28	94.06
	HRDFuse	0.3141	0.3090	0.4867	0.1331	70.72	87.94	93.89
	GLPanoDepth	0.5028	0.4539	0.6992	0.1800	52.66	76.25	87.68
	ASNGeo	0.2954	0.2469	0.4595	0.1224	73.75	89.87	94.92
	Ours	0.2053	0.1684	0.3428	0.0940	82.79	93.63	96.74
	Ours-Improved by	20.46%	21.64%	17.06%	17.69%	7.54	2.54	1.13
Ours Average Improvement		21.57%	23.14%	12.65%	16.75%	4.28	1.32	0.58

semantic segmentation. We preprocessed the dataset, forming examples in an 8:1:1 ratio, resulting in 2,181 test data instances with randomly selected lighting conditions.

4.4 Implementation Details

Our experiments were conducted using a single CPU core of an Intel Xeon W-2133 along with an RTX 3090 GPU. The batch size was 2, and the input resolution was 256×512 . We employed the Adam optimizer with default settings, initialising the learning rate to 10^{-4} and decreasing it by half every 12 epochs. The training process extended to 120

epochs, with early stopping implemented at the 12th epoch if no further improvements were achieved.

4.5 Experimental Results

For both tasks, we conducted a quantitative comparison between our proposed model and state-of-the-art methods across the five datasets, as detailed in Tables 1 and 2. To ensure a fair evaluation, we retrained all models using their own authors’ hyper-parameter settings and identical data splits. Our method consistently outperformed existing approaches for both tasks, setting a new state-of-the-art across all five benchmarks.



Table 2 360° surface normal comparisons on five benchmarks. We compare our method to state-of-the-art approaches, highlighting improvements over existing best results for each error and accuracy metric as 'Ours-improved by'.

* Indicates evaluation performed using the corresponding partitions of the 3D60 dataset.

Dataset	Method	Error metric ↓			Accuracy metric ↑				
		Mean	Median	MSE	δ_{N1}	δ_{N2}	δ_{N3}	δ_{N4}	δ_{N5}
3D60	UniFuse	6.5829	0.5169	268.6102	76.09	78.82	82.46	89.59	92.28
	PanoFormer	17.2109	6.4281	906.0848	50.72	55.15	60.70	72.83	78.10
	OmniFusion	7.7549	1.3175	301.8934	72.35	76.01	80.2	88.22	91.26
	HyperSphere	5.6176	0.2421	215.0301	77.34	79.99	83.84	91.11	93.71
	ASNGeo	32.8173	28.0937	1214.0923	0.03	0.04	0.06	0.46	64.11
	Ours	5.2394	0.3025	187.1651	78.19	81.25	85.12	91.85	94.35
	Ours-improved by	6.73%	-24.94%	12.96%	0.85	1.27	1.28	0.73	0.64
Stanford2D3D*	UniFuse	6.9502	0.4675	297.777	76.34	78.77	82.21	88.57	91.29
	PanoFormer	17.2017	7.2088	849.7950	48.21	52.98	59.04	72.13	78.08
	OmniFusion	8.0590	1.2903	322.0786	72.42	76.14	80.31	87.46	90.47
	HyperSphere	6.0463	0.2242	244.3175	77.48	79.76	83.26	89.73	92.49
	ASNGeo	33.3921	28.4364	1263.7831	0.04	0.06	0.09	0.39	60.84
	Ours	5.7956	0.3222	219.0471	77.74	80.27	83.77	90.29	93.02
	Ours-Improved by	4.15%	-43.7%	10.31%	0.26	0.51	0.51	0.56	0.53
Matterport3D*	UniFuse	7.2675	0.6434	289.4016	72.91	76.04	80.22	88.59	91.62
	PanoFormer	18.1228	7.3137	944.5936	47.56	52.20	58.10	71.21	76.84
	OmniFusion	8.500	1.5493	327.3145	69.16	73.08	77.75	87.06	90.49
	HyperSphere	6.2324	0.3041	231.6290	74.13	77.23	81.70	90.29	93.23
	ASNGeo	33.3434	28.3574	1254.0368	0.03	0.04	0.06	0.45	61.06
	Ours	5.7579	0.3677	199.5677	75.29	78.92	83.42	91.20	93.99
	Ours-Improved by	7.61%	-20.94%	13.84%	1.16	1.69	1.72	0.91	0.77
SunCG*	UniFuse	3.3994	0.0416	154.5543	89.01	90.31	91.98	94.75	95.92
	PanoFormer	13.6272	2.3037	805.9224	65.38	68.63	72.32	79.80	83.06
	OmniFusion	4.3822	0.3854	177.3558	85.51	87.96	90.25	93.75	95.22
	HyperSphere	2.6630	0.0031	118.1888	90.46	91.61	93.22	95.83	96.86
	ASNGeo	30.0883	26.6731	1001.082	0	0	0	0.59	79.91
	Ours	2.5345	0.0067	103.0089	90.58	91.84	93.45	96.07	97.11
	Ours-Improved by	4.83%	-116.08%	12.84%	0.12	0.23	0.23	0.24	0.25
Structured3D	UniFuse	10.4186	0.7087	576.2404	70.99	76.28	78.91	84.11	86.66
	PanoFormer	20.2634	8.6808	1157.807	47.02	52.68	58.12	68.7	73.75
	OmniFusion	12.0589	2.0627	634.7285	65.79	71.9	75.67	82.02	85.04
	HyperSphere	9.4531	0.2763	517.8832	72.76	77.73	79.81	84.97	87.62
	ASNGeo	36.2867	30.3338	1538.0035	0.01	0.01	0.01	0.12	53.12
	Ours	8.9783	0.4831	469.0207	72.51	77.87	80.65	86.02	88.58
	Ours-Improved by	5.02%	-74.87%	9.44%	-0.25	0.14	0.84	1.05	0.96
Ours Average Improvement		5.88%	-49.91%	11.20%	0.30	0.71	1.06	0.89	0.80

Specifically, for 360° depth estimation, it demonstrated an average improvement of 21.57% in MAE, 23.14% in ARE, 12.65% in RMSE, and 16.75% in RMSElog, surpassing previous best-performing depth estimation methods. For 360° surface normal prediction, it achieved a 5.88% improvement in mean error and 11.20% in MSE, although with a higher median error of 49.91% on average (see our discussion of limitations in Sec. 4.9).

Our model demonstrated a significant performance advantage across all benchmarks for the depth estimation task. Specifically, it achieved substantial improvements of 22.67%,

24.64%, and 15.80% on 3D60; 20.56%, 22.16%, and 13.22% on Stanford2D3D; 23.22%, 26.03%, and 17.04% on Matterport3D; and 24.97%, 16.67%, and 14.41% on SunCG for MAE, ARE, and RMSElog, respectively. These lower error metrics indicate that our model produces more accurate and reliable depth maps, reducing discrepancies between predicted and actual depths. On the surface normal prediction task, our model also showed considerable improvement, with gains of 6.73% and 12.96% on 3D60; 4.15% and 10.31% on Stanford2D3D; 7.61% and 13.84% on Matterport3D; and 4.83% and 12.84% on SunCG for the mean and MSE error

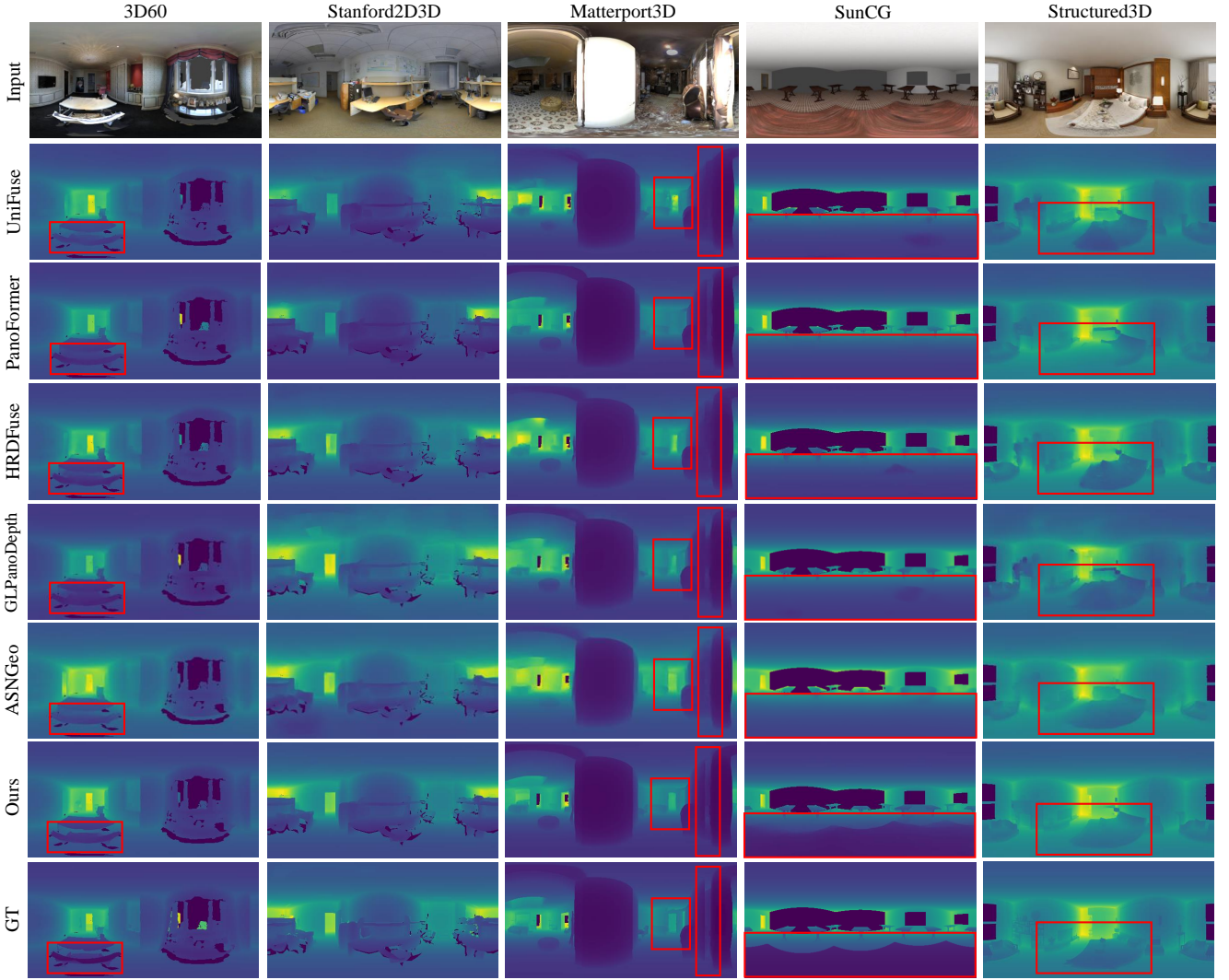


Fig. 4 Qualitative 360° depth comparisons were conducted on diverse datasets including 3D60 [14], Stanford2D3D [45], Matterport3D [46], SunCG [47], and Structured3D [44]. Areas outlined in red are regions where our approach notably enhances object boundaries, providing a more accurate representation of the overall scene geometry. GT denotes ground truth.

metrics, respectively. These improvements indicate that our model delivers more precise surface orientation information, resulting in a deeper understanding of the scene's geometry. This highlights our MTL architecture's effectiveness, which simultaneously enhances both tasks. The lower error metrics for depth and surface normal estimation reflect a more accurate reconstruction of scene depth and finer surface detail recognition. These advances demonstrate the superior performance of our model to that of state-of-the-art methods, establishing it as a new benchmark for 360° image geometric estimation.

To assess the generalization ability of our MTL model, we applied the models trained on the 3D60 dataset directly to the Structured3D dataset, revealing a significant performance gap between our model and others. While UniFuse demonstrated

strong generalization for the depth task, our model surpassed it by 20.46% for MAE, and 21.64% for ARE, and achieved a 7.54% higher accuracy score for depth predictions within a difference of 1.25 from the ground truth. For the surface normal task, our model outperformed HyperSphere, which previously exhibited the best performance. Specifically, our model showed a 5.02% lower mean error, and a 9.44% lower MSE error, but slightly decreased accuracy (0.25) for angular differences with ground truth under 5°. These differences can be attributed to Structured3D's synthetic nature, featuring a unique depth range distribution and a mix of small objects with subtle depth and surface changes, like cups, alongside significant depth variations, such as hollow shelves with books. The limitations of previous methods, which focused exclusively on feature representations learned from the single

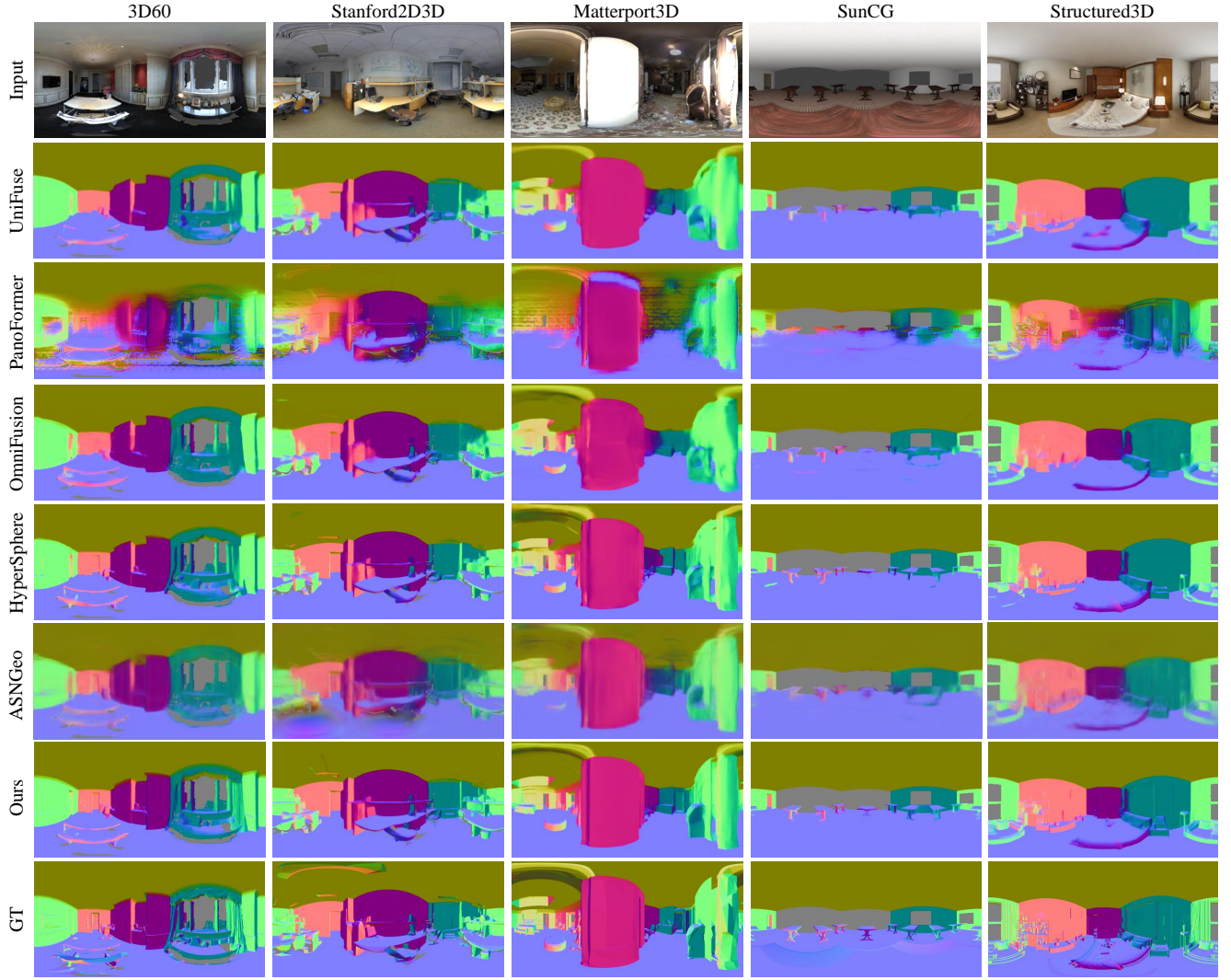


Fig. 5 Qualitative 360° surface normal comparisons between HyperSphere [23], ASNGeo [3], the adapted UniFuse [8], PanoFormer [10], OmniFusion [9] and our method.

task, became evident in their reduced generalization ability and effectiveness across diverse datasets. Our MTL architecture addresses these challenges, enhancing the adaptability and robustness of our model to various scenarios and different datasets.

To provide a comparison to another MTL method, we applied a recent MTL method designed for perspective images, ASNGeo [3], to directly handle 360° data for both depth and surface normal estimation. Quantitative results show that ASNGeo consistently underperforms across all five benchmarks, delivering worse results than other methods. This outcome underscores the limitations of directly applying perspective-based MTL architectures to the 360° domain, where they fail to adequately address the unique challenges posed by spherical distortion and the non-uniform spatial relationships inherent in panoramic imagery. These findings highlight the

effectiveness of our proposed MTL architecture specifically designed for 360° imagery. Unlike perspective-based methods, our approach successfully adapts to the unique geometric properties of panoramic images, resulting in significantly better performance and demonstrating the critical need for specialized solutions in the 360° domain.

We present qualitative comparisons for each task for various methods in Figs. 4 and 5, showing results from a single test instance for each of the five benchmarks. For the depth task, we highlight critical regions in red rectangles to emphasize the differences between our method and existing approaches. Our model consistently captures finer details, rendering sharper and more complete object boundaries within the scenes. Notably, our model exhibits a superior understanding of the geometric structure, as demonstrated by the Stanford2D3D example, where it accurately captures the scale and propor-

tions of the entire scene with reduced color discrepancies compared to other methods. In the qualitative comparison for surface normals, we visualize the predicted normal vectors, with invalid areas represented in gray. Our model outperforms state-of-the-art methods by providing more accurate representations of geometric structures and surface orientations, further illustrating its effectiveness in enhancing scene understanding and geometric perception.

4.6 Computational Effort

To investigate the extra computational cost of using a multi-task approach, we compared computation times for our model and PanoFormer [10] on an RTX3090; see Table 3. Our multi-task model requires more computational resources (262.38 GFLOPs, 130.32 GMACs) than PanoFormer (151.63 GFLOPs, 74.85 GMACs) due to its multi-task nature, which simultaneously predicts both depth and surface normals. This increase in computational demand is expected in models that handle multiple tasks, as they inherently require more parameters and operations to integrate and process additional information. Despite the higher complexity, our model maintained a comparable training speed (49 min/epoch) to PanoFormer (47.5 min/epoch) on the 3D60 dataset. The inference time for a single frame differs by less than 10% (0.1212 sec/instance for our model vs. 0.1109 sec/instance for PanoFormer), indicating that the additional task does not impose a substantial delay in real-time applications.

However, in resource-constrained environments such as mobile devices or embedded systems, where computational power and memory are limited, the model’s increased complexity may pose challenges. To mitigate this, we could optimize the model in terms of architecture and training strategies. Architecturally, we could adapt PanoFormer’s block to capture global dependencies on lower-resolution feature maps while using convolutional neural network blocks to extract high-resolution features. This approach reduces computational overhead while preserving the model’s ability to process the complex geometric information in 360° imagery. On the training side, we could implement PyTorch’s mixed precision training, which significantly reduces memory usage and training time. By selectively using full precision where necessary, this method minimizes memory footprint while maintaining high accuracy. It is especially effective on modern hardware, such as NVIDIA GPUs, which have dedicated support for mixed precision operations.

While these optimizations could improve the efficiency of our model, additional trade-offs must be considered for

Table 3 Computational Effort.

	GFLOPs	GMACs	Training Time	Inference Time
PanoFormer	151.63	74.85	47.5 min / epoch	0.1109 s
Ours	262.38	130.32	49 min / epoch	0.1212 s

Table 4 Ablation study.

Method	MAE ↓	ARE ↓	RMSE ↓
Baseline	0.1577	0.0787	0.2975
Baseline+FB	0.1295	0.0649	0.2470
Baseline+FB+Fusion	0.1458	0.0742	0.2682
Baseline+FB+Multi-scale	0.0997	0.0480	0.2110
Ours (all components)	0.0962	0.0465	0.2050

deployment in low-resource environments. For example, techniques such as pruning, quantization, or distillation could further reduce resource usage, although they often come at the cost of accuracy. In scenarios where inference speed is critical but high precision is not, these methods may be employed to strike a better balance between performance and resource constraints. Overall, our current implementation demonstrates that, despite its higher complexity, the model remains feasible for environments with moderate computational resources, such as high-end consumer GPUs or cloud-based systems.

4.7 Ablation Study

We conducted an individual component study on the 3D60 dataset to validate the critical components of our multi-task architecture under consistent training and testing conditions: see Table 4. Our baseline model duplicated the PanoFormer network for both depth and surface normal tasks, with the two branches only intersecting at the bottleneck block. This configuration has unsatisfactory performance, indicating that a naive combination of networks does not suffice for effective multi-task learning. To evaluate other components of our MTL model, we introduced a shared convolutional feature extraction block (FB) for both branches to extract low-level features. This modification led to a notable improvement of 17.88% in terms of MAE.

Next, we investigated the effectiveness of the fusion blocks and the multi-scale decoder within the existing structure. While these components led to improvements of 7.55% and 36.78%, respectively, adding the fusion module alone slightly reduced performance compared to using only the feature embedding block. This is likely due to the increased complexity of shared task information, which the network struggles to process efficiently without the multi-scale decoder to balance and integrate information across different levels. The fusion module is designed to facilitate knowledge transfer between tasks, but without the multi-scale decoder, it cannot fully capitalize on this synergy. However, when all components

Table 5 Quantitative comparison of different fusion strategies for depth and surface normals on the 3D60 dataset.

Method	Depth Estimation				Surface Normal Estimation			
	MAE ↓	ARE ↓	RMSE ↓	$\delta_{D1} \uparrow$	Mean ↓	Median ↓	MSE ↓	$\delta_{N1} \uparrow$
One encoder	0.0984	0.0474	0.2087	97.59	5.4010	0.3594	193.7227	77.92
Cross-attention	0.1026	0.0496	0.2141	97.32	5.3561	0.3442	192.6810	78.08
Ours	0.0962	0.0465	0.2050	97.66	5.2394	0.3025	187.1651	78.19

were integrated into our comprehensive multi-task architecture, performance improved by 39.00%, demonstrating how the fusion module and multi-scale decoder complement each other to enhance results for both tasks. This outcome underscores the importance of each component of our multi-task network and highlights how their combined effect is crucial to achieving the reported performance.

4.8 Alternative Architectures

We further conducted experiments on two alternative fusion module designs: (i) using a shared encoder for both depth and surface normal estimation, and (ii) applying a cross-domain attention mechanism in the decoder to bridge the gap between the two tasks. Our proposed fusion module still outperforms these alternatives in both depth and surface normal estimation, as reported in Table 5.

4.8.1 Shared Encoder for Both Tasks

In the first experiment, we used a single shared encoder for both tasks. This approach (One encoder) has the advantage of reducing the overall number of parameters and simplifying the model architecture. However, while this strategy achieved acceptable results, especially for the depth estimation task, it could not fully differentiate between the specific characteristics of depth and surface normal features. Each task requires different feature representations, particularly in the early stages of encoding, where distinct geometric cues are crucial for accurate predictions. The shared encoder was unable to capture these nuances effectively, leading to weaker surface normal estimation performance. The error metrics show that this approach led to an imbalance between the tasks, with the depth task dominating the other during training, which limited the model's ability to generalize well across both tasks simultaneously.

4.8.2 Cross-Domain Attention in the Decoder

The second experiment involved using a cross-domain attention mechanism to bridge depth and surface normal estimation in the decoder stage. While this design (Cross-attention) was intended to enhance information exchange between the two tasks during decoding, it introduced excessive complexity to the model. The resulting architecture became too large

Table 6 Examples from (a) Stanford2D3D and (b) SunCG datasets.

Example	Method	Mean ↓	Median ↓	MSE ↓
(a)	HyperSphere	15.1213	2.6880	715.2992
	Ours	14.3891	5.0646	601.8008
(b)	HyperSphere	6.4296	0.2639	146.5674
	Ours	3.1416	0.4131	75.3159

to train at full scale, significantly increasing computational demands and memory requirements. As a result, we did not apply cross-attention at the final scale. The results in Table 5 show that this strategy caused one task to dominate the other during training. Surface normal estimation achieved better quantitative results than depth estimation, indicating an imbalance in task performance.

4.8.3 Our Fusion Module

In contrast, our proposed fusion module achieved an appropriate balance between the two tasks by facilitating smooth information transfer without overwhelming the network with excessive complexity. The separate encoders allow for task-specific feature extraction, and the fusion module effectively shares useful information between the two branches without leading to overfitting or imbalance in the training for each task. As a result, both tasks achieve their best results simultaneously. This demonstrates the effectiveness of our fusion module and the entire architecture for maintaining high performance across both depth and surface normal estimation.

4.9 Limitations and Future Work

Our model provides new state-of-the-art performance for 360° depth estimation across all metrics, and for 360° surface normal estimation across most metrics except median error, as shown in Table 2. For 360° surface normal estimation, we primarily compared our model to the current state-of-the-art, HyperSphere, and consistently observed lower mean and MSE metrics, although a higher median error. Individual quantitative results from the Stanford2D3D (example (a)) and SunCG (example (b)) datasets are detailed in Table 6. The low mean error values reflect that, on average, our model's predictions are more closely aligned to true surface orientations than HyperSphere's (3.1416 versus 6.4296 in example (b)). The low MSE, which penalizes larger errors more heavily,

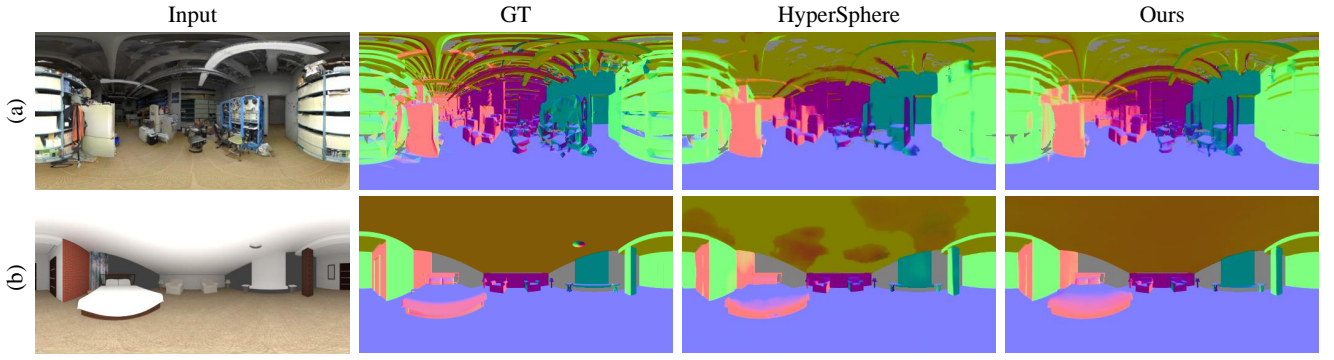


Fig. 6 Qualitative evaluation on two specific examples from the Stanford2D3D (a) and SunCG (b) datasets. Our model demonstrates more precise predictions, accurately capturing object boundaries and the entire ceiling.

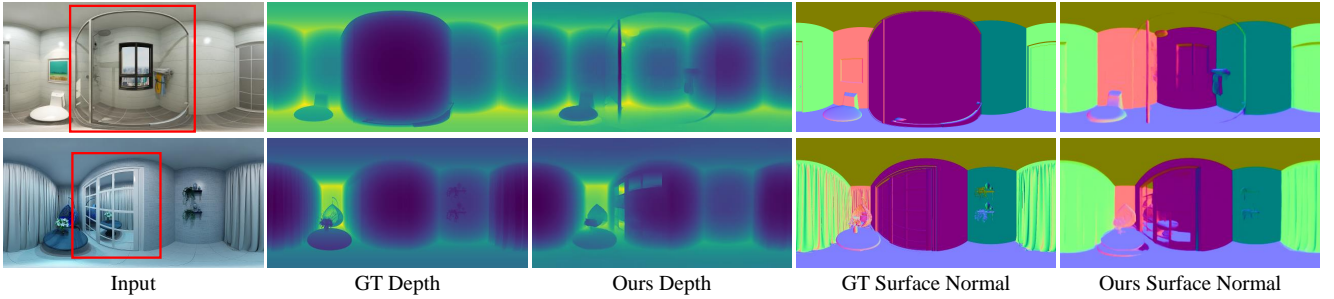


Fig. 7 Failures involving glass walls (above) and mirrors (below) from the Structured3D dataset. Red rectangles indicate relevant regions.

further suggests that our model avoids significant outliers, ensuring stable and accurate predictions across most of the image (601.8008 versus 715.2992 in example (a)).

However, the higher median error indicates challenges with specific outliers or complex regions (5.0646 versus 2.6880 in example (a), and 0.4131 versus 0.2639 in example (b)). We visualize these examples in Fig. 6, where our method captures more geometric details around small object boundaries in (a) and accurately predicts the ceiling’s surface normals, whereas HyperSphere struggles in (b). While the consistently low mean and MSE errors highlight our model’s effectiveness in delivering accurate surface normal predictions across a wide range of scenarios, the higher median error points to areas for future improvement. Specifically, addressing the occasional difficulties our model faces with outliers and certain challenging regions will be a key focus in our future work.

Additionally, our model encounters issues when dealing with scenes containing glass walls or mirrors, as illustrated in Fig. 7. In such scenarios, the model often struggles to accurately interpret surface orientations and depth due to the unique visual effects introduced by these materials. For instance, mirrors can reflect entire sections of a room, causing the model to perceive over-extended scene depth and misinterpret surface normals. This occurs because the model

treats the reflection as a continuation of the physical environment, resulting in erroneous geometric predictions. Similarly, when transparent glass is present in front of the camera, the model may over-extrapolate depth or surface normal values by mistakenly interpreting the space behind the glass as part of the scene geometry, despite the distortion caused by the transparency.

To address these limitations, future research could explore strategies to handle reflective and transparent surfaces. One potential solution is incorporating additional material-based cues to allow the model to differentiate between glass, mirrors, and solid objects. This could involve using reflectance maps or leveraging external sensors that detect surface properties beyond visual data. Another approach could include semantic segmentation in the multi-task framework, enabling the model to identify and treat reflective or transparent objects differently during depth and surface normal estimation. These enhancements would make the model more robust in practical applications, such as indoor navigation and scene reconstruction, where these materials are common.

5 Conclusions

In this paper, we proposed an MTL network for monocular indoor 360° geometric estimation, achieving state-of-the-art performance for both depth and surface normal tasks simultaneously. Our architecture leverages the strengths of MTL to

provide a comprehensive understanding of scene geometry by effectively fusing features from both depth and surface normal estimations. We introduced a fusion module composed of specifically designed blocks to facilitate positive knowledge transfer between the two ViT branches. Additionally, our multi-scale spherical decoder further enhances the perception of scene structure at various levels. Experimental results demonstrate that our approach establishes new baselines for both tasks, highlighting our model's superior performance, robustness and generalization ability. This is further evidenced by conducting experiments on the Structured3D dataset, underscoring its potential applicability to real-world scenarios.

Declarations

Availability of Data and Materials

The training and testing datasets are publicly available online. The code and model are available at <https://github.com/huankun101230/360MTLGeometricEstimation>.

Competing interests

The authors have no competing interests to declare that are relevant to the content of this article.

Funding

This research was supported by the Marsden Fund Council managed by the Royal Society of New Zealand under Grant No. MFP-20-VUW-180 and the Royal Society (UK) under Grant No. IES\RI\180126.

Authors' Contributions

K. Huang designed and developed the deep architecture, conducted the experiments, and wrote the paper. K. Huang and F.-L. Zhang initiated the project and the collaboration. F.-L. Zhang contributed to the method design, experiment design and paper editing. F. Zhang contributed to the method design and paper editing. Y.-K. Lai and P. Rosin contributed to the method design and experiment design. N.A. Dodgson contributed to the method design and paper editing.

Acknowledgements

We thank the funding agencies for supporting this work, as detailed above.

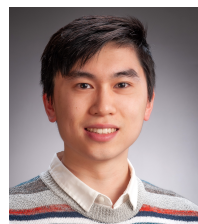
References

- [1] Liu S, Johns E, Davison AJ. End-To-End Multi-Task Learning With Attention. In *Proceedings of the IEEE/CVF Conference on Computer Vision and Pattern Recognition (CVPR)*, 2019.
- [2] Standley T, Zamir A, Chen D, Guibas L, Malik J, Savarese S. Which Tasks Should Be Learned Together in Multi-task Learning? In HD III, A Singh, editors, *Proceedings of the 37th International Conference on Machine Learning*, volume 119 of *Proceedings of Machine Learning Research*, 2020, 9120–9132.
- [3] Long X, Zheng Y, Zheng Y, Tian B, Lin C, Liu L, Zhao H, Zhou G, Wang W. Adaptive surface normal constraint for geometric estimation from monocular images. *IEEE Transactions on Pattern Analysis and Machine Intelligence*, 2024.
- [4] Liao S, Gavves E, Snoek CG. Spherical Regression: Learning viewpoints, surface normals and 3d rotations on n-spheres. In *Proceedings of the IEEE/CVF Conference on Computer Vision and Pattern Recognition*, 2019, 9759–9767.
- [5] Coors B, Condurache AP, Geiger A. SphereNet: Learning spherical representations for detection and classification in omnidirectional images. In *Proceedings of the European conference on computer vision (ECCV)*, 2018, 518–533.
- [6] Wang FE, Yeh YH, Sun M, Chiu WC, Tsai YH. BiFuse: Monocular 360° depth estimation via bi-projection fusion. In *Proceedings of the IEEE/CVF Conference on Computer Vision and Pattern Recognition*, 2020, 462–471.
- [7] Wang FE, Yeh YH, Tsai YH, Chiu WC, Sun M. BiFuse++: Self-supervised and efficient bi-projection fusion for 360° depth estimation. *IEEE Transactions on Pattern Analysis and Machine Intelligence*, 2022, 45(5): 5448–5460.
- [8] Jiang H, Sheng Z, Zhu S, Dong Z, Huang R. UniFuse: Uni-directional fusion for 360° panorama depth estimation. *IEEE Robotics and Automation Letters*, 2021, 6(2): 1519–1526.
- [9] Li Y, Guo Y, Yan Z, Huang X, Duan Y, Ren L. OmniFusion: 360 monocular depth estimation via geometry-aware fusion. In *Proceedings of the IEEE/CVF Conference on Computer Vision and Pattern Recognition*, 2022, 2801–2810.
- [10] Shen Z, Lin C, Liao K, Nie L, Zheng Z, Zhao Y. PanoFormer: Panorama Transformer for Indoor 360° Depth Estimation. In *European Conference on Computer Vision*, 2022, 195–211.
- [11] Ai H, Cao Z, Cao YP, Shan Y, Wang L. HRDFuse: Monocular 360° Depth Estimation by Collaboratively Learning Holistic-With-Regional Depth Distributions. In *Proceedings of the IEEE/CVF Conference on Computer Vision and Pattern Recognition*, 2023, 13273–13282.
- [12] Zhuang C, Lu Z, Wang Y, Xiao J, Wang Y. ACDNet: Adaptively combined dilated convolution for monocular panorama depth estimation. In *Proceedings of the AAAI Conference on Artificial Intelligence*, volume 36, 2022, 3653–3661.
- [13] Sun C, Sun M, Chen HT. HoHoNet: 360 indoor holistic understanding with latent horizontal features. In *Proceedings of the IEEE/CVF Conference on Computer Vision and Pattern Recognition*, 2021, 2573–2582.
- [14] Zioulis N, Karakottas A, Zarpalas D, Daras P. OmniDepth: Dense depth estimation for indoors spherical panoramas. In *Proceedings of the European Conference on Computer Vision (ECCV)*, 2018, 448–465.

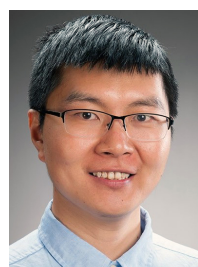
- [15] Bai J, Qin H, Lai S, Guo J, Guo Y. GLPanoDepth: Global-to-local panoramic depth estimation. *IEEE Transactions on Image Processing*, 2024.
- [16] Rey-Area M, Yuan M, Richardt C. 360MonoDepth: High-resolution 360° monocular depth estimation. In *Proceedings of the IEEE/CVF Conference on Computer Vision and Pattern Recognition*, 2022, 3762–3772.
- [17] Ai H, Wang L. Elite360D: Towards Efficient 360 Depth Estimation via Semantic-and Distance-Aware Bi-Projection Fusion. In *Proceedings of the IEEE/CVF Conference on Computer Vision and Pattern Recognition*, 2024, 9926–9935.
- [18] Liu J, Xu Y, Li S, Li J. Estimating Depth of Monocular Panoramic Image with Teacher-Student Model Fusing Equirectangular and Spherical Representations. In *Proceedings of the IEEE/CVF Conference on Computer Vision and Pattern Recognition*, 2024, 1262–1271.
- [19] Long X, Lin C, Liu L, Li W, Theobalt C, Yang R, Wang W. Adaptive surface normal constraint for depth estimation. In *Proceedings of the IEEE/CVF international conference on computer vision*, 2021, 12849–12858.
- [20] Bae G, Budvytis I, Cipolla R. Estimating and exploiting the aleatoric uncertainty in surface normal estimation. In *Proceedings of the IEEE/CVF International Conference on Computer Vision*, 2021, 13137–13146.
- [21] Chen Z, Shen Y, Ding M, Chen Z, Zhao H, Learned-Miller EG, Gan C. Mod-Squad: Designing Mixtures of Experts As Modular Multi-Task Learners. In *Proceedings of the IEEE/CVF Conference on Computer Vision and Pattern Recognition (CVPR)*, 2023, 11828–11837.
- [22] Do T, Vuong K, Roumeliotis SI, Park HS. Surface normal estimation of tilted images via spatial rectifier. In *Computer Vision–ECCV 2020: 16th European Conference, Glasgow, UK, August 23–28, 2020, Proceedings, Part IV 16*, 2020, 265–280.
- [23] Karakottas A, Zioulis N, Samaras S, Ataloglou D, Gkitsas V, Zarpalas D, Daras P. 360° surface regression with a hyper-sphere loss. In *2019 International Conference on 3D Vision (3DV)*, 2019, 258–268.
- [24] Zhang F, Mei Y, Nguyen S, Tan KC, Zhang M. Task Relatedness-Based Multitask Genetic Programming for Dynamic Flexible Job Shop Scheduling. *IEEE Transactions on Evolutionary Computation*, 2022, 27(6): 1705–1719.
- [25] Guizilini V, Lee KH, Ambrus R, Gaidon A. Learning optical flow, depth, and scene flow without real-world labels. *IEEE Robotics and Automation Letters*, 2022, 7(2): 3491–3498.
- [26] Zhao H, Zhang J, Zhang S, Tao D. JPPerceiver: Joint perception network for depth, pose and layout estimation in driving scenes. In *European Conference on Computer Vision*, 2022, 708–726.
- [27] Mayer N, Ilg E, Hausser P, Fischer P, Cremers D, Dosovitskiy A, Brox T. A large dataset to train convolutional networks for disparity, optical flow, and scene flow estimation. In *Proceedings of the IEEE conference on computer vision and pattern recognition*, 2016, 4040–4048.
- [28] Kendall A, Gal Y, Cipolla R. Multi-task learning using uncertainty to weigh losses for scene geometry and semantics. In *Proceedings of the IEEE conference on computer vision and pattern recognition*, 2018, 7482–7491.
- [29] Bhanushali J, Muniyandi M, Chakravarthula P. Cross-Domain Synthetic-to-Real In-the-Wild Depth and Normal Estimation for 3D Scene Understanding. In *Proceedings of the IEEE/CVF Conference on Computer Vision and Pattern Recognition*, 2024, 1290–1300.
- [30] Saxena S, Herrmann C, Hur J, Kar A, Norouzi M, Sun D, Fleet DJ. The surprising effectiveness of diffusion models for optical flow and monocular depth estimation. *Advances in Neural Information Processing Systems*, 2024, 36.
- [31] Liu H, Lu T, Xu Y, Liu J, Wang L. Learning optical flow and scene flow with bidirectional camera-lidar fusion. *IEEE Transactions on Pattern Analysis and Machine Intelligence*, 2023.
- [32] Liu M, Wang S, Guo Y, He Y, Xue H. Pano-SfMLearner: Self-Supervised multi-task learning of depth and semantics in panoramic videos. *IEEE Signal Processing Letters*, 2021, 28: 832–836.
- [33] Dong Y, Fang C, Bo L, Dong Z, Tan P. PanoContext-Former: Panoramic Total Scene Understanding with a Transformer. In *Proceedings of the IEEE/CVF Conference on Computer Vision and Pattern Recognition (CVPR)*, 2024, 28087–28097.
- [34] Xu D, Ouyang W, Wang X, Sebe N. PAD-Net: Multi-tasks guided prediction-and-distillation network for simultaneous depth estimation and scene parsing. In *Proceedings of the IEEE conference on computer vision and pattern recognition*, 2018, 675–684.
- [35] Wang Y, Tsai YH, Hung WC, Ding W, Liu S, Yang MH. Semi-supervised multi-task learning for semantics and depth. In *Proceedings of the IEEE/CVF Winter Conference on Applications of Computer Vision*, 2022, 2505–2514.
- [36] Kundu JN, Lakkakula N, Babu RV. UM-Adapt: Unsupervised multi-task adaptation using adversarial cross-task distillation. In *Proceedings of the IEEE/CVF International Conference on Computer Vision*, 2019, 1436–1445.
- [37] Sun X, Panda R, Feris R, Saenko K. AdaShare: Learning what to share for efficient deep multi-task learning. *Advances in Neural Information Processing Systems*, 2020, 33: 8728–8740.
- [38] Chen Z, Badrinarayanan V, Lee CY, Rabinovich A. GradNorm: Gradient normalization for adaptive loss balancing in deep multitask networks. In *International conference on machine learning*, 2018, 794–803.
- [39] Ruder S. An overview of multi-task learning in deep neural networks. *arXiv preprint arXiv:1706.05098*, 2017.
- [40] Yuan K, Guo S, Liu Z, Zhou A, Yu F, Wu W. Incorporating convolution designs into visual transformers. In *Proceedings of the IEEE/CVF International Conference on Computer Vision*, 2021, 579–588.
- [41] Ioffe S, Szegedy C. Batch Normalization: Accelerating deep

- network training by reducing internal covariate shift. In *International conference on machine learning*, 2015, 448–456.
- [42] Luo P, Ren J, Peng Z, Zhang R, Li J. Differentiable Learning-to-Normalize via Switchable Normalization. *International Conference on Learning Representation (ICLR)*, 2019.
- [43] Simonyan K, Zisserman A. Very deep convolutional networks for large-scale image recognition. *arXiv preprint arXiv:1409.1556*, 2014.
- [44] Zheng J, Zhang J, Li J, Tang R, Gao S, Zhou Z. Structured3D: A large photo-realistic dataset for structured 3d modeling. In *Computer Vision–ECCV 2020: 16th European Conference, Glasgow, UK, August 23–28, 2020, Proceedings, Part IX 16*, 2020, 519–535.
- [45] Armeni I, Sax S, Zamir AR, Savarese S. Joint 2d-3d-semantic data for indoor scene understanding. *arXiv preprint arXiv:1702.01105*, 2017.
- [46] Chang A, Dai A, Funkhouser T, Halber M, Niessner M, Savva M, Song S, Zeng A, Zhang Y. Matterport3D: Learning from RGB-D data in indoor environments. *arXiv preprint arXiv:1709.06158*, 2017.
- [47] Song S, Yu F, Zeng A, Chang AX, Savva M, Funkhouser T. Semantic scene completion from a single depth image. In *Proceedings of the IEEE conference on computer vision and pattern recognition*, 2017, 1746–1754.

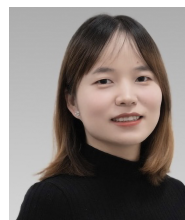
Author biographies



Kun Huang is currently a Ph.D. candidate at Victoria University of Wellington, New Zealand. He received bachelor's and M.S. degrees from Victoria University of Wellington in 2017 and 2021, respectively. His research interests include 360° image and video editing, computer vision, virtual reality and mixed reality. He is a student branch chair and professional activity coordinator of the IEEE New Zealand Central Section.



Fang-Lue Zhang received a Ph.D. degree from Tsinghua University in 2015. He is currently a Senior Lecturer in Computer Graphics at the Victoria University of Wellington. His research interests include image and video editing, computer vision, and computer graphics. He received a Victoria Early-Career Research Excellence Award in 2019, and a Fast-Start Marsden Grant from the New Zealand Royal Society in 2020. He is on the editorial board of Computers & Graphics. He served as program chair of Pacific Graphics 2020 & 2021, and CVM 2024. He is a committee member of IEEE Central New Zealand Section.



Fangfang Zhang received a Ph.D. degree in computer science from Victoria University of Wellington in 2021. Her Ph.D. thesis received an IEEE CIS Outstanding Ph.D. Dissertation Award. She is currently a lecturer in the Centre for Data Science and Artificial Intelligence & School of Engineering and Computer Science, Victoria University of Wellington.

Her research interests include evolutionary computation, hyper-heuristic learning/optimisation, job shop scheduling, surrogates, and multitask learning. She is an Associate Editor of Expert Systems With Applications, and Swarm and Evolutionary Computation. She is the secretary of the IEEE New Zealand Central Section, and Vice-Chair of the IEEE Taskforce on Evolutionary Scheduling and Combinatorial Optimisation.



Yu-Kun Lai Yu-Kun Lai is a Professor in the School of Computer Science and Informatics, Cardiff University, UK. He received his B.S. and Ph.D. degrees in computer science from Tsinghua University in 2003 and 2008 respectively. His research interests include computer graphics, computer vision, geometric modeling, and image processing.



Paul L. Rosin Paul L. Rosin is a Professor in the School of Computer Science and Informatics, Cardiff University. He received his Ph.D. degree from City University, London, in 1988. Previous posts were at Brunel University, the Institute for Remote Sensing Applications, Joint Research Centre, Italy, and Curtin University of Technology. His research interests include low-level image processing, performance evaluation, shape analysis, facial analysis, medical image analysis, 3D mesh processing, cellular automata, non-photorealistic rendering, and cultural heritage.



Neil Dodgson Neil Dodgson is Professor of Computer Graphics and Dean of Graduate Research at Victoria University of Wellington. His Ph.D. was in image processing, from the University of Cambridge, where he spent 25 years, becoming full Professor in 2010. His research is in 3D TV, subdivision surfaces, imaging, and aesthetics. He is a Fellow of Engineering New Zealand, of the Institution of Engineering and Technology and of the Institute for Mathematics and its Applications.